Carbon 225 (2024) 119145

Contents lists available at ScienceDirect

Carbon

journal homepage: www.elsevier.com/locate/carbon

Graphene conductance modulation through controlled molecular release in a hybrid coordination polymer/graphene field-effect transistor

Lucía Martín-Pérez [a], Esther Resines-Urien [a], José Sánchez Costa [a,**], Enrique Burzurí [b,c,a,*]

[a] IMDEA Nanociencia C/Faraday 9 Ciudad Universitaria de Cantoblanco, 28049, Madrid, Spain
[b] Departamento de Física de La Materia Condensada, Universidad Autónoma de Madrid, E-28049, Madrid, Spain
[c] Condensed Matter Physics Center (IFIMAC) and Instituto Universitario de Ciencia de Materiales "Nicolás Cabrera" (INC), Universidad Autónoma de Madrid, E-28049, Madrid, Spain

ARTICLE INFO

Keywords:
Coordination polymers
Hybridization
Graphene
Electronic devices
Structural transformations

ABSTRACT

Coordination polymers, including metal-organic frameworks (MOFs), present a wide range of functionalities ranging from sensing to energy storage. Despite this, many coordination polymers are typically insulating which prevents their implementation into nanoscale electronic devices. Besides, the hybridization of MOFs with other conducting materials, like graphene, is rather unexplored. Here we introduce the grafting of a soft non-porous coordination polymer, the **1**·2CH_3CN, on a single-layer graphene to form a hybrid **1**·2CH_3CN/graphene field effect transistor. Electron transport measurements show that the sharp structural transformations in **1**·2CH_3CN, triggered at two specific temperatures, are detected in graphene as two sharp increments in the electrical current. Gate spectroscopy measurements show that the origin of the electrical modulation is an abrupt p-doping due to the sudden release of acetonitrile right at the structural transition temperatures. Reciprocally, the sensitivity of graphene to external perturbations allows to detect additional transformations in the coordination polymer not observed in direct transport measurements across crystals. Finally, the results have been reproduced in *in-situ* grown **1**·2CH_3CN nanoscale films on CVDG FETs. This simple method optimizes the contact area between graphene and **1**·2CH_3CN and facilitates the integration of coordination polymers with van der Waals materials and electronic devices. Further, a selective doping at specific temperatures could be obtained by modifying the nature of the interstitial molecule in **1**.

1. Introduction

Crystalline coordination polymers (CPs) are a large family of materials in which metal cations are linked together by organic ligands to form 1, 2 or 3-dimensional polymers. These polymers organize in crystals *via* a combination of coordinative covalent bonds and supramolecular interactions which confer stability to the atomic network. The absence (or presence) of pores capable of hosting molecules and the stiffness of the material divides crystalline coordination polymers into porous coordination polymers (pCPs), also named as metal-organic frameworks (MOFs) [1], and non-porous coordination polymers (npCPs) [2,3], some of the latter with the ability to act as porous.

The wide diversity of compatible building blocks (ligands and metal) provides CP with properties like luminescence [4], magnetism [5,6] and magnetic switching [7,8], gas/vapor absorption [9], sensing [10,11], and energy storage [12], among others. Despite this appealing range of functionalities, coordination polymers and, more generally, (metal) organic crystals face two key challenges for their implementation into nano-electronic devices. The first is the insulating nature of many of these materials [13]. In recent years a large improvement in conductivity has been achieved by introducing charge delocalization, conjugation, π-π hybridization and the selection of the metal [13–19]. An alternative approach may consist in merging coordination polymers with a more conducting matrix that, in turn, may allow to combine different functionalities in a hybrid material. The second major challenge is to find geometries in which typically fragile and insoluble coordination polymers, coupled to other conducting matrices, are compatible with nanoscale electronic devices and fabrication processes.

Van der Waals materials [20], like graphene, offer an interesting path to tackle both challenges. Graphene provides a robust, flexible and

* Corresponding author. Departamento de Física de la Materia Condensada, Universidad Autónoma de Madrid, E-28049, Madrid, Spain.
** Corresponding author.
E-mail addresses: jose.sanchezcosta@imdea.org (J.S. Costa), enrique.burzuri@uam.es (E. Burzurí).

https://doi.org/10.1016/j.carbon.2024.119145
Received 11 October 2023; Received in revised form 8 April 2024; Accepted 12 April 2024
Available online 16 April 2024

conducting surface whose electronic properties can be modulated by external stimuli. Besides, graphene has been implemented in a large number of complex electronic devices [21,22] and coupled with other materials. To cite some, graphene-based transistors have been developed as electronic sensors to deposited spin-crossover nanoparticles [23], thin films [24,25] and molecular crystals [26], other 2D materials [20,27] and biomolecules [28], among many others. Variations in different physical properties of the adsorbate (spin state, volume, permittivity) are translated into a distinct electronic response in graphene. Reciprocally, graphene not only "senses" but its electronic properties can be selectively modulated with these external materials.

The electronic coupling between CP and graphene is less explored. In general, MOFs do not exhibit significant structural transformations nor sharp transitions, such as spin-crossover coordination polymers, that could be sensed by graphene or modify its electronic properties. As a result, most reports focus on advantages for electrochemistry, catalysis [29] and energy storage [30] but do not explore electron transport. Besides, most of these reports use CP-graphene composites [31] not compatible with nanoscale fabrication. A recent pioneering work reports the exfoliation of a spin-crossover MOF and its deposition on graphene [8]. The change in volume associated to the spin crossover transition induces strain in graphene thus changing its resistance. This approach largely facilitates the integration of MOFs into nanoscale devices whereas on the other hand it is limited to cleavable coordination polymers. Besides, this report, focused on spin crossover (SCO) materials, does not explore the most defining property of MOFs, *i.e.* their ability to dynamically interact with small molecules.

Non-porous coordination polymers (npCP) acting as porous can be an interesting, largely unexplored alternative for hybridization with graphene. npCPs can accommodate or release small molecules from their structure *via* internal lattice reorganization, which confers a high degree of selectivity [2,3,32]. The guest molecules, typically weakly coupled to the polymer, can migrate across the crystal and produce complex molecular dynamics [33,34]. Besides, npCP are usually softer materials than MOFs. Softness and molecular dynamics in npCPs may be key to achieve a deeper hybridization with graphene and other van der Waals materials that may enable to sense molecular dynamics in the crystal and, in turn, to controllably modify the electronic properties of graphene.

Here we report the grafting of a non-porous coordination polymer, **1**·2CH_3CN, on single-layer graphene to form a hybrid **1**·2CH_3CN/graphene field effect transistor. We show that the sharp structural transformations triggered at two specific temperatures in the crystal are sensed by graphene as two sharp increments in the electrical current at the transition temperatures. Gate spectroscopy measurements in solid-state devices reveal that the change in current is caused by a large and abrupt p-doping caused by the sudden release of acetonitrile molecules from the crystal lattice, concomitant with the structural transitions. Moreover, the high sensitivity of graphene's band structure to alterations in the mechanical and electrostatic environment have allowed to detect additional structural transitions in **1**·2CH_3CN not observed in direct transport measurements contacting crystals [33,34].

Finally, we have in-situ grown **1**·2CH_3CN thin films on CVDG FETs by drop-casting of the reaction mixture in solution. We show that **1**·2CH_3CN crystallizes with an identical crystalline phase and preserves the structural and optical transitions of macroscopic single crystals grown in solution. This simple method optimizes the contact area between graphene and **1**·2CH_3CN and facilitates the integration of coordination polymers with van der Waals materials and electronic devices.

2. Methods

Materials: Chemicals and reagents were purchased from commercial suppliers and used as received. CVDG was fabricated in the cleanroom facilities at IMDEA Nanociencia.

Synthesis of compound ***1**·2CH_3CN* ($_\infty${[$Fe(H_2O)_2(CH_3CN)_2$(pyrazine)]$(BF_4)_2$·$(CH_3CN)_2$}(**1**·2CH_3CN) *and* ($_\infty${[$Fe(H_2O)_2(CH_3CN)_2$(pyrazine)]$(BF_4)_2$}): Compound **1**•2CH_3CN was synthetized at room temperature, dissolving $Fe(BF_4)_2$·6H_2O (0.64 mmol) in acetonitrile (2.5 mL) and adding it drop by drop to a solution of pyrazine (1.2 mmol) in acetonitrile (2.5 mL). The resulting solution was stirred for 15 min and filtered. After one day, yellow crystals appeared. See additional details in Ref. [34] The compound **1** was obtained by heating up **1**•2CH_3CN.

X-ray Diffraction Spectroscopy: Powder X-ray diffraction data was collected in a Rigaku Smartlab SE diffractometer with a Bragg-Brentano configuration, using Cu-Kα radiation (λ = 0.1541 nm). The sample was measured between 5° and 50° with a speed of 1.8° min^{-1} under an X-Ray fluorescence reduction mode, at room temperature.

Optical Reflectivity: Optical Reflectivity measurements were performed using a MOTIC SMZ-171 optical stereoscope coupled with a MOTICAM 3. Images were collected in BMP format without any filter using the Motic Images Plus 3.0 software, with the mean value from each region of interest (ROI) analysed under the ImageJ program. The temperature was controlled using a Linkam T95 system controller and a LPE 95 Liquid Nitrogen Cooling System.

Raman Spectroscopy: Raman spectra were recorded with a Bruker Senterra confocal Raman microscope (Bruker Optic, Ettlingen, Germany, resolution 3 cm^{-1}) using the following parameters: objective NA 0.75, x50; laser excitation: 532 nm, 2 mW, 10 coadditions, 2 s integration time. The temperature was controlled using a Linkam T95 system controller and a LPE 95 Liquid Nitrogen Cooling System. The resulting spectra come from the average of 3–5 measurements acquired on a certain region.

Electron Transport Measurements: The current–voltage curves, current–temperature and gate characteristics are obtained in a range of temperatures between RT and 363 K in the chamber of a Lakeshore Cryogenics (Model PS-100 Tabletop) probe station (Z70 microscope vision system, STC-HD93DV (Omron Sentech, (Kanagawa, Japan)) camera), equipped with a Keithley 2450 digital source-meter unit, a Tenma 72–270 Programmable DC Power Supply (60 V, 3 A) and a Lakeshore Temperature Cryogenic Controller Model 336.

Device fabrication details: The pristine graphene field-effect transistors (p-CVDG GFETs) were fabricated *via* laser mask-less optical lithography and thermal evaporation of Cr/Au (5/80 nm) electrodes onto a CVDG graphene layer grown in a highly-doped silicon substrate capped with a 90 nm thick insulating SiO_2 layer, used as common back-gate electrode. First, Si/SiO_2 wafers were cleaned using *i*PrOH and acetone to remove any traces of organic, ionic and metallic impurities. After that, AZ 1505 positive photoresist is spin coated at 5000 rpm for 1 min onto the surface followed by baking at 90 °C for 1 min to form a 450 nm resist layer. The electrodes and pads are defined by exposing the surface to UV light using a Heidelberg Instruments (Heidelberg, Germany) DWL66fs laser writer of 405 nm (h-line) with 300 mJ/cm^2 dose. The pattern is subsequently developed with AZ 351B. Thereafter 5 nm Cr and 80 nm Au layers were deposited using Ecovac e-beam evaporation by Angstrom Engineering (Kitchener, Canada). A lift-off process in acetone/*i*PrOH/deionized water removes the excess metallic material. A second lithography step was carried out to etch graphene from unwanted areas and to create a graphene channel between the electrodes. Negative photoresist AZ nLof 2070 was used to protect the graphene bridge between electrodes and the rest was exposed to oxygen plasma to etch. Finally, this resist was removed with acetone. The dimension of the graphene channel created was 200 × 200 μm^2. The devices were annealed at 300 °C for 8h after the fabrication. This fabrication was performed at IMDEA Nanociencia clean room facilities. Target crystals (4.5–5 mm long and 0.5–06 mm wide) are positioned by mechanical manipulation. First, a needle tip (0.80 × 120mm) is used to manually move the crystal from the solution to the surface area as close as possible to the graphene FET. Thereafter, micrometric precision on the placement is achieved by pulling/pushing the crystal with the conducting tips of the electrical probe station.

Graphene preparation: Graphene is grown on a copper (Cu) film using

chemical vapor deposition (CVD). The cleaned Cu substrate is placed inside a CVD chamber and the gas precursors are introduced. The chamber is heated to a high temperature (800–1000 °C). Following the desired growth duration and formation of graphene layers, the chamber is gradually cooled down.

To transfer CVD-grown graphene onto a silicon wafer, the silicon wafer is initially thoroughly cleaned to remove any contaminants and residues. A sacrificial layer of PMMA is spin-coated onto the graphene/Cu substrate. The Cu substrate is then etched away using a solution of ammonium persulfate (APS) and water (50 mL/50 mL) for 2–3 h. Following the Cu etching, the sample undergoes two washing cycles in water. Next, the PMMA/graphene stack, floating on the water surface, is carefully transferred onto the silicon wafer. The PMMA layer is dissolved using acetone (for approximately 10 min), leaving the graphene transferred onto the silicon wafer. Finally, the wafer is washed with isopropyl alcohol and carefully cleaned with N_2 gas.

3. Results and discussion

3.1. 1·2CH_3CN/CVDG hybrid formation and characterization

The **1**·2CH_3CN, short for [$_\infty$[Fe(H_2O)$_2$(CH_3CN)$_2$(pyrazine)](BF_4)$_2$·(CH_3CN)$_2$] npCP crystals, are synthesized as previously detailed [34]. See an optical image of the crystal in Fig. 1a. **1**·2CH_3CN crystals are formed by closely packed 1D coordination chains in which the Fe core is hexacoordinated with two pyrazine, two acetonitrile, and two water molecules as seen in Fig. 1b. See Ref. [34] and Fig. S1 in the Supporting Information for additional information on the crystal structure. In addition, **1**·2CH_3CN contains two uncoordinated acetonitrile molecules coupled to the polymer chains through hydrogen bonds formed with the coordinated water molecules. No weakly bonded water molecules are found in the lattice structure [34]. Two sharp structural transitions in the crystal were reported at $T_I \approx 310$ K and $T_{II} \approx 350$ K [33,34], concomitant with the desorption of the uncoordinated acetonitrile molecules from the crystal lattice (blue shaded molecules in Fig. 1b), leading to the **1** crystal (Fig. 1a). The breaking of van der Waals bonds of interstitial acetonitrile, and irreversible loss of the molecules from the lattice, is accompanied by sharp peaks in the conductance of the crystal and crystal colour change from yellow to orange.

The pristine graphene field-effect transistors (p-CVDG FETs) were fabricated *via* laser mask-less optical lithography and thermal evaporation of Cr/Au (5/80 nm) electrodes onto a CVDG graphene layer grown on a Si/SiO_2 substrate. The highly-doped silicon substrate is used as a back-gate electrode. A second lithography step was carried out to etch graphene from unwanted areas and to create a graphene channel (200 μm × 200 μm) between the electrodes. Finally, the devices were annealed at 300 °C for 8h. See Fig. 1a for an optical image of a representative device and Experimental Section for additional details.

The structural and crystal transformation properties of graphene and **1**·2CH_3CN are studied after forming the **1**·2CH_3CN/CVDG hybrid FET. Fig. S3a in the Supporting Information shows the Raman spectra measured on the p-CVDG FET and the same device after placing the

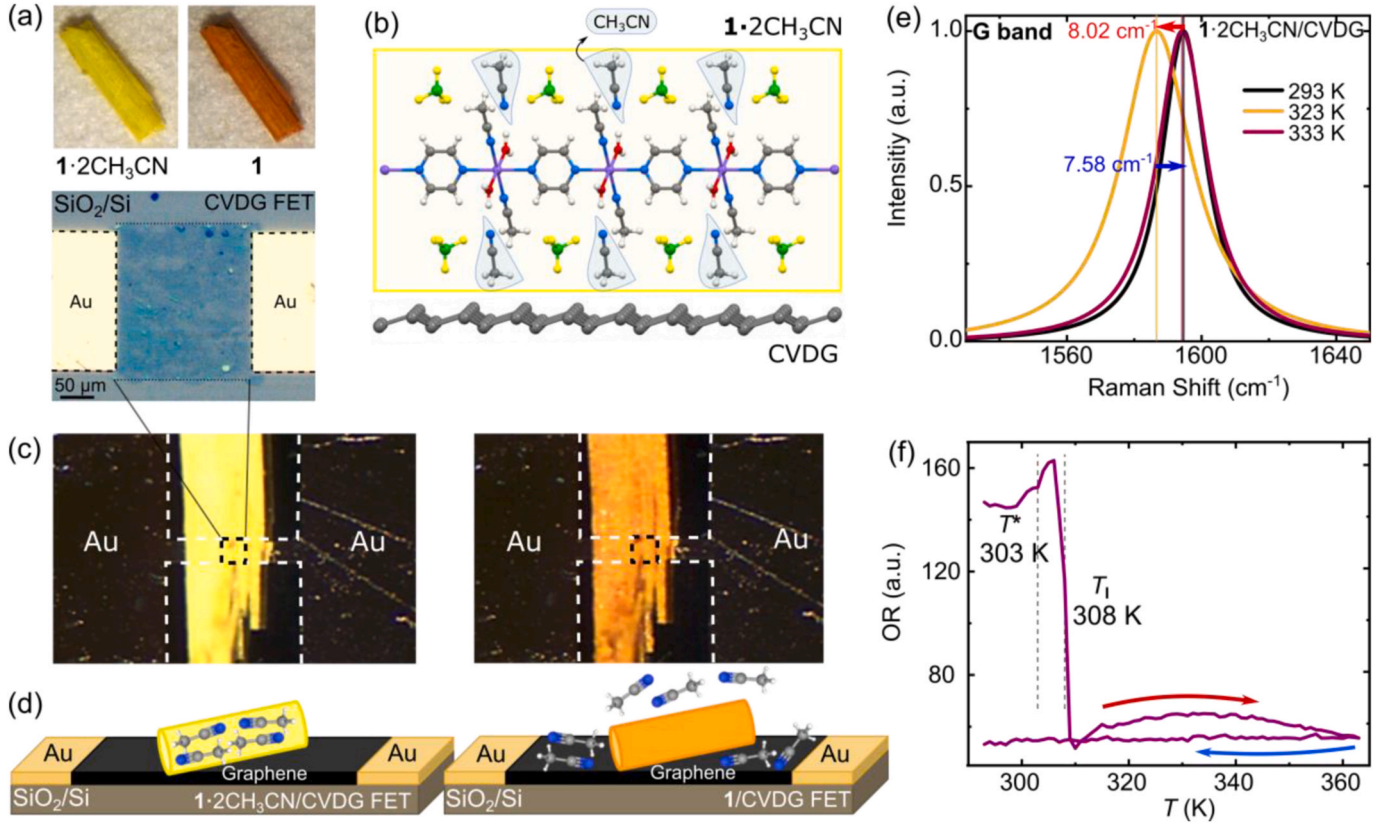

Fig. 1. a) Top: Optical images of a **1**·2CH_3CN crystal at room temperature (left) and the same crystal after temperature-induced crystal transformation and subsequent loss of acetonitrile molecules (**1**, right). Bottom: Representative p-CVDG FET with a 200 μm × 200 μm graphene bridge before placing the **1**·2CH_3CN crystal. b) Atomic representation of the **1**·2CH_3CN/CVDG hybrid. The pyrazine chains in the crystal, with weakly-bonded CH_3CN molecules (shaded), lie parallel to the graphene surface. Color scheme: Fe (violet), N (blue), C (grey), O (red), H (white), B (green), F (yellow). c) Optical images of a **1**·2CH_3CN/CVDG FET (left) and a **1**/CVDG FET after acetonitrile release (right). The dashed square indicates the position of the CDVG FET under the crystal. d) Schematic representation of the crystal transformation in the **1**·2CH_3CN/CVDG FET. Acetonitrile is released modifying the graphene surface. e) G-band Raman spectra (λ_{exc} = 532 nm) measured on a **1**·2CH_3CN/CVDG FET at different temperatures. A sharp redshift (−8.02 cm^{-1}) is observed at T_{III} = 323 K followed by a subsequent blueshift (+7.58 cm^{-1}) at higher temperatures. This behaviour is not observed in p-CVDG FET (See Fig. S3 in the Supporting Information). f) Optical reflectivity of a **1**·2CH_3CN crystal coated onto the device (**1**·2CH_3CN/CVDG FET) measured between 293 K and 363 K.

1·2CH_3CN crystal. The Raman spectra measured in the **1**·2CH_3CN/CVDG hybrid are taken on the exposed graphene at the edge with the crystal since the crystal is thick enough to block the Raman signal underneath. The main Raman bands in graphene appear upshifted in energy by around 2.5 cm^{-1} after the crystal is placed on top. A Raman blueshift on carbon-based materials has been associated to strain or chemical doping by electron-acceptor molecules [26,35].A stronger Raman shift may be present on the graphene directly under the crystal where doping or strain induced by the crystal is expected to be more intense. In the **1**·2CH_3CN/CVDG structure, strain on graphene could be induced by the crystal whereas doping could be caused by initial acetonitrile molecules from the liquid matrix. Acetonitrile is a known electron withdrawer molecule [36]. Besides, no significant increment in the D band is observed. This band is typically associated to the disruption of the sp^2 hybridization by defects in the lattice (see Fig. S2 in the Supporting Information).

Fig. 1f shows the optical reflectivity (OR) measured on the **1**·2CH_3CN/CVDG FET as a function of the temperature. A small increment in the OR concomitant with an increased crystal brightness is observed at $T^* = 303$ K. Thereafter OR abruptly drops at $T_I \approx 308$ K and the crystal colour shifts from yellow to dark orange (Fig. 1c), in agreement with previous reports in isolated **1**·2CH_3CN crystals [33,34]. The colour change is associated to a structural transition that releases non-coordinated acetonitrile molecules from the crystal into the environment [33,34], as shown in Fig. 1d.

3.2. Electrical measurements

The effect of the crystal transformation and the release of acetonitrile on graphene is explored in electron transport measurements. The large difference in conductivity between graphene and the **1**·2CH_3CN coordination polymer (more than three orders of magnitude) [33,34] and the ohmic Au/graphene contact promotes charge transport mainly through graphene in the final hybrid device. All electron transport measurements are performed in atmospheric conditions.

Fig. 2a shows the current I – source-drain voltage V_{sd} characteristics measured on a pristine graphene (p-CVDG) FET and the same device (Sample 1) after placing a **1**·2CH_3CN crystal to form the **1**·2CH_3CN/CVDG hybrid FET (Fig. 1c). The current through graphene approximately doubles after the **1**·2CH_3CN crystal is coupled on top. Thereafter the temperature is ramped up from room temperature (297 K) up to 363 K, that is, covering the two main structural transitions (*I* and *II*) observed in isolated **1**·2CH_3CN crystals [33,34]. The temperature sweeping step is set to a constant $\Delta T = 1$ K. The conductance steadily increases with increasing temperature. An ohmic-like conductance is preserved throughout all the temperature range. Besides, two clear jumps in current appear at 306 K and 321 K (black arrows in the inset of Fig. 2a) symmetric at positive and negative bias.

A better insight on the thermal evolution of the conductance can be gained by fixing V_{sd}. Fig. 2b shows the current measured as a function of the temperature at $V_{sd} = 2$ V in a second **1**·2CH_3CN/CVDG hybrid FET (Sample 2). The relative change in current ΔI (297 K → 363 K) = 137 % is considerably larger than that observed for the same p-CVDG FETs without the crystal (7 %, black line in Fig. 2b). See Fig. S5 in the

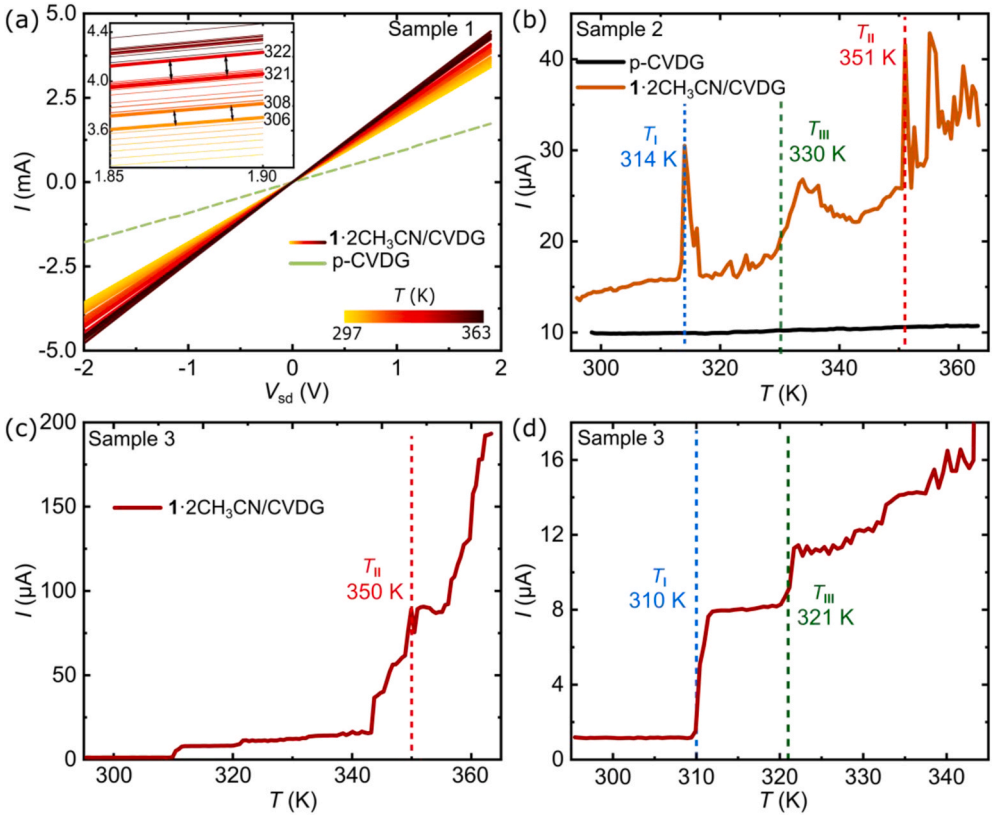

Fig. 2. Electrical characterization of **1**·2CH_3CN/CVDG-FETs. a) Temperature-dependent current–voltage (I–V_{sd}) characteristics measured on a p-CVDG FET and the same device after deposition of a **1**·2CH_3CN crystal to form the hybrid **1**•2CH_3CN/CVDG-FET (Sample 1). The temperature is increased from 293 K to 363 K with a $\Delta T = 1$ K step. The inset is a zoom in the high-bias area. b) Current–temperature (I–T) characteristic measured on a second **1**·2CH_3CN/CVDG-FET (Sample 2). The source-drain voltage is fixed to $V_{sd} = 2$V. Three clear peaks in current appear at around $T_I = 314$ K, $T_{II} = 351$ K and $T_{III} = 333$ K. T_I and T_{II} coincide in temperature with the structural transitions reported for isolated **1**·2CH_3CN crystals [33,34]. The black line corresponds to the pristine device (p-CVDG FET) before placing the **1**·2CH_3CN. c) I–T characteristic measured on a third **1**·2CH_3CN/CVDG-FET (Sample 3). A zoom on the low temperature region is shown in d). A series of plateaus appear at temperatures comparable to Sample 2. All measurements are performed at $V_g = 0$. (A colour version of this figure can be viewed online.)

Supporting Information. Remarkably, two large jumps in graphene conductance appear at $T_I = 314$ K and $T_{II} = 351$ K. These temperature values roughly match with the structural transitions *I* and *II* observed in the isolated **1**•2CH_3CN crystals [33,34]. Charge carriers in graphene therefore sense the single-crystal-to-single-crystal transformations taking place in the non-porous coordination polymer crystal coupled to it.

Remarkably, a third peak shows up in current in the $T_{III} = 320$–330 K range, as seen in Fig. 2b, that is roughly reproducible from sample to sample. See Fig. 2d and Fig. S6 in the Supporting Information for additional devices. The appearance of this third peak in conductance is additionally associated to an abrupt redshift of the G band in graphene at T_{III}, as observed in temperature-dependent Raman spectroscopy in Fig. 1e, pointing to a change in the vibrational spectrum of graphene at that temperature. This peak has not been detected previously in the isolated **1**•2CH_3CN crystal [34] nor has been observed in p-CVDG FETs (see also Fig. S3b in the Supporting Information).

Fig. 2c shows the current thermal evolution measured on an additional **1**•2CH_3CN/CVDG FET (Sample 3). A zoom in on the lower temperature region (293 K < *T* < 345 K) is shown in Fig. 2d. The appearance of sharp transitions in graphene conductance is reproducible at roughly the same temperatures. The relative change in the current is comparable or even larger than those reported for chemo-electrical gating of graphene with SCO crystals [26] and other MOFs [8]. Besides, the conductance at the transition temperature is, in absolute terms, three orders of magnitude larger than by measuring directly on the crystal [33,34]. This greatly simplifies the incorporation of typically insulating non-porous coordination polymers into electronic devices.

Interestingly, a subtle difference arises between Sample 2 and Sample 3. While Sample 3 shows plateaus right after the transitions in the crystal, Sample 2 shows peaks instead after which the conductance decreases back to pre-transition values. Both behaviours (plateaus and peaks) are repeatedly observed in different samples. See Fig. S6 in the Supporting Information. This duality may be indicative of a different dynamic interaction between acetonitrile and graphene at the crystal transition temperature. Acetonitrile is a very volatile compound. Different **1**•2CH_3CN crystal shapes and contact geometry with graphene may, tentatively, determine acetonitrile release (from the crystal onto graphene) and surface evaporation (from graphene to ambient) rates, leading to fast (slow) evaporations and therefore peaks (plateaus).

We now discuss the possible mechanisms able to couple the crystal-to-crystal transformation into a distinct conductance in graphene. The lattice reorganization in the non-porous **1**•2CH_3CN crystal, triggered specifically at T_I and T_{II}, is concomitant with the release of weakly-bonded acetonitrile molecules from the lattice into the surrounding media [34]. See schematics in Fig. 1b and d. These crystal and molecular dynamics may open three different scenarios for the underlying graphene. First, acetonitrile is known to be an electron acceptor [36,37]. Therefore p-doping of graphene by released acetonitrile is a plausible mechanism explaining the increment in current (Fig. 1d). Alternatively, the release of acetonitrile modifies the crystal relative permittivity ε [33], effectively modifying the dielectric properties around graphene. This may lead to a chemo-electrical gating of graphene similar to that observed for spin-crossover crystals deposited on 2D materials [26]. Finally, mechanical strain cannot be discarded either [8]. **1**•2CH_3CN crystals undergo a significant volume reduction (26 %) after the acetonitrile is evacuated from the lattice [34] that could in turn modify the strain on the graphene lattice. Note that the change in the magnetic properties of the paramagnetic **1**•2CH_3CN crystals is too subtle to induce a significant effect in graphene [34].

To gain a deeper knowledge on the nature of the conductance jumps and the different scenarios described before, we explored the graphene energy landscape by applying a gate voltage (V_g) to the silicon substrate underneath the **1**•2CH_3CN/CVDG hybrid. The gate voltage shifts the Fermi energy in graphene. Fig. 3a shows the current as a function of V_g measured at a fixed bias $V_{sd} = 2$ V and room temperature before (p-CVDG; black curve) and after (**1**•2CH_3CN/CVDG; light purple curve) placing the crystal on top of graphene in Sample 1. The ambipolar (electron-hole) behavior characteristic of the Dirac cone-like band structure in graphene is observed in the p-CVDG FET. The cone reaches a minimum, the charge neutrality point, at $V_{cnp} = 20$ V indicating a slight p-doping of the initial pristine graphene device. This initial doping has been typically ascribed to the presence of impurities from the CVDG production or the fabrication of the devices [38–40]. The coupling of the **1**•2CH_3CN crystal to graphene induces a further cone shift of $\Delta V_g = 30$ V towards positive gate voltages. This shift is signature of a further p-doped graphene. The residual carrier density per area *n* increases from n(p-CVDG) = $4.92 \cdot 10^{12}$ cm^{-2} to n(**1**•2CH_3CN/CVDG) = $1.20 \cdot 10^{13}$ cm^{-2} (See Section S4 in the Supporting Information for details). Note that no significant modification of the current at the cone minimum is observed. The graphene lattice is therefore roughly preserved and no major defects seem to be formed by placing the **1**•2CH_3CN crystal on top [40]. These results support the conclusions from the Raman spectroscopy analysis (See Supporting Information).

Thereafter, the I–V_g characteristics are measured by ramping up the temperature from 273 K up to 363 K (Fig. 3a–c). Additionally, the position of the charge neutrality point as function of the temperature is

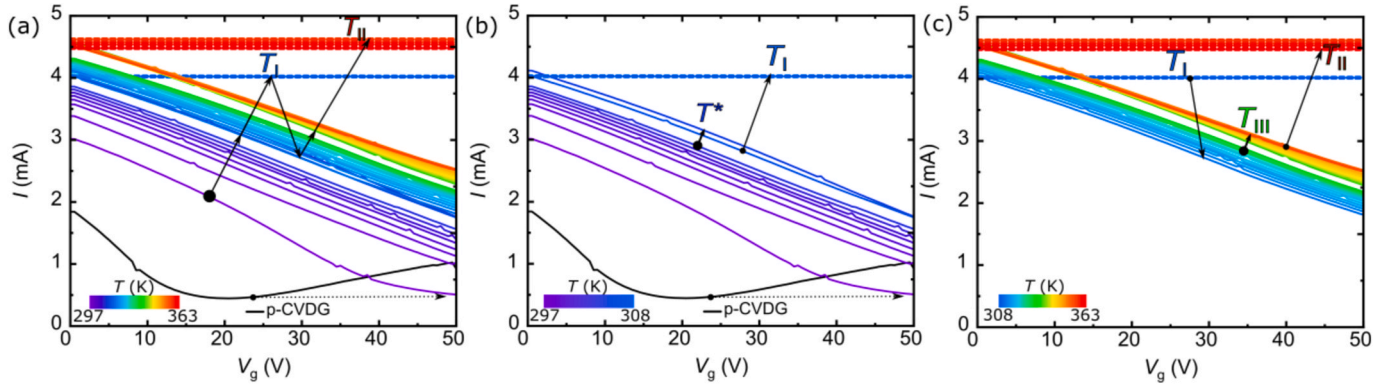

Fig. 3. a) Temperature-dependent current I – gate voltage V_g characteristics measured at a fixed source-drain voltage $V_{sd} = 2$ V on a **1**•2CH_3CN/CVDG FET (coloured lines, Sample 1). The black curve corresponds to the pristine device (p-CVDG FET) before placing the crystal on top. An initial p-doping on graphene (dotted horizontal arrow from black to purple) is observed after placing the crystal. Thereafter, the cone smoothly shifts to higher energies with temperature. Two sharp transitions, in which current becomes independent of gate voltage, are observed at $T_I = 308$ K and $T_{II} = 357$ K (horizontal dashed lines), i.e. the structural transition temperatures of the **1**•2CH_3CN crystal. This behaviour indicates a sudden, strong p-doping of graphene concomitant with the crystal transitions in **1**•2CH_3CN. b,c) Same measurement as in a) but separated in a low temperature range (297–308 K, (b)) and a high temperature range (308K −363 K (c)) for clarity. Two additional small jumps can be observed at $T^* = 305$ K, and $T_{III} = 322$ K not reported before for **1**•2CH_3CN. (A colour version of this figure can be viewed online.)

shown in Fig. 4d. Note that the cone tip lies beyond safe gate values for the device (>50 V). The charge neutrality point is therefore roughly estimated from the hole branch and assuming a constant minimum current at the tip, as explained in Section S5 in the Supporting Information.

Initially, the charge neutrality point gradually shifts towards more positive V_g and thus, a larger p-doping of graphene. The opposite trend is reported for p-CVDG FETs where the desorption of water molecules from graphene leads to a shift of the charge neutrality point to more negative V_g [41]. An initial gradual release of electron acceptor [36] acetonitrile from the crystal onto graphene seems therefore a more plausible scenario.

Remarkably at T_I = 308 K, *i.e.* the first structural transition in the crystal, the current becomes independent of V_g (Fig. 3b) and seems to be close to the hole transport saturation limit starting to show up at $V_g = 0$. The charge neutrality point has thus moved to much larger energy values. A lower-limit boundary has been represented in Fig. 4d (dot in the blue stripe). By further increasing the temperature, doping decreases and the hole carrier gating and the gradual increment with temperature is recovered until the second crystal structural transition temperature T_{II} = 357 K is reached (Fig. 3c). There, a new gate-independent and temperature-independent current-saturation regime is reached, with no clear signs of gate-tunability recovery at the highest measured temperatures. The sharp temperature-induced shift observed in these measurements seems to support an abrupt p-doping of graphene triggered by the transient release of acetonitrile molecules in the crystal, as schematically shown in Fig. 4a–c.

Transitions T_I and T_{II} can also be clearly observed by measuring the current as a function of the temperature in the same Sample 1 at different V_g values (colour scale), as shown in Fig. 4e. All the $I(V_g)$ curves collapse to the $I(V_g = 0)$ value and become independent of the gate voltage. The relative change in current at T_I and T_{II} transitions can be therefore maximized or tuned by increasing V_g. This property is relevant to maximize graphene sensitivity when used as a detector.

Interestingly, two additional small steps appear at T^* = 305 K (Fig. 3b) and at T_{III} = 322 K (Fig. 3c), also visible as a small V_g shift of the charge neutrality point in Fig. 4d and e. The former appears right before the first transition (T_I) and coincides in temperature with the increment in brightness and OR observed for **1**•2CH_3CN in Fig. 1, whereas the latter step agrees in temperature with the T_{III} step observed in Fig. 2. In contrast to T_I and T_{II}, these additional steps do not reach a saturation regime (Fig. 3b and c) and their magnitude does not seem to depend on V_g (Fig. 4e), which may be indicative of a different mechanism involving a lower or no doping by acetonitrile release from the crystal. This scenario is supported by the fact that neither T^* nor T_{III} are detected in direct electron transport measurements in isolated crystals [33,34].

Alternatively, the change in conductance at $T^*$and T_{III} may be partially induced by mechanical strain on graphene as a result of the crystal transformation. A similar strain-induced shift of the Fermi level has been reported for SCO crystals deposited on graphene [8,26].

Temperature dependent Raman spectroscopy in the **1**•2CH_3CN/CVDG shows a significant G band redshift (~-8 cm^{-1}) concomitant with a 2D band blueshift (~+4 cm^{-1}) in graphene right at T_{III}, as shown in Fig. 1e and Fig. S4 respectively). Note that a further p-doping would in contrast lead to a blueshift in G [42]. This relative shift between G and 2D bands seems to point to a combined doping and compressive strain mechanism as detailed elsewhere [42]. The compressive strain could be understood in terms of a shrinking crystal, previously observed when the crystal loses acetonitrile [34]. The same compressive strain mechanism has been proposed for shrinking SCO crystals on graphene [8].

Therefore we tentatively ascribe T^* and T_{III} to a combined doping and compressive strain induced by structural transitions in **1**·2CH_3CN. Note that a deeper understanding and disentanglement of the relative weights between doping and strain requires a dedicated Raman study on this issue, as shown in Ref. [42].

The former transition may be associated to a crystal transformation

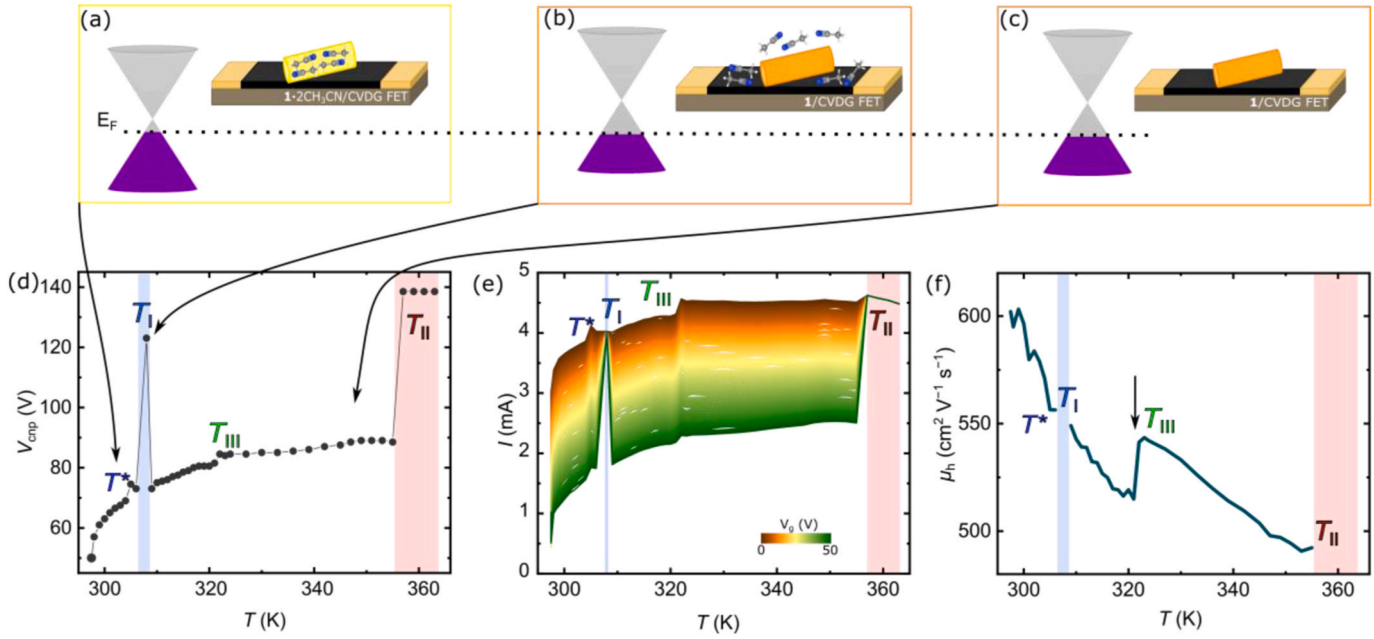

Fig. 4. (a–c) Schematics of the **1**·2CH_3CN/CVDG FET and graphene Dirac cone at three different temperatures: (a) Below T_I, acetonitrile is bond to the **1**•2CH_3CN lattice and only slight p-doping is observed, (b) The structural transition in the crystal at T_I abruptly releases the interstitial acetonitrile inducing a large p-doping in graphene. (c) Above T_I, acetonitrile partially evaporates returning the Fermi level to approximately pre-transition values. (d) Charge neutrality point position (V_{cnp}) as a function of the temperature. The cone shifts to higher voltages with increasing temperature with large jumps at T_I and T_{II}. The V_{cnp} values at T_I and T_{II} are lower boundaries for V_{cnp}. Besides the transitions at T_I and T_{II}, two additional shifts in the cone position appear at T^* = 305 K and T_{III} = 322 K. e) I–T characteristics at different V_g, represented from the data shown in Fig. 3a). The current becomes independent of V_g at T_I and T_{II}, involving a larger current jump the larger V_g. In contrast, the magnitude of the jump is independent of V_g for T^* and T_{III}. f) Field-effect hole mobility (μ_h) as function of temperature. μ_h decreases with increasing temperature as expected for graphene. A sharp increment in μ_h is observed for T_{III} (black arrow). (A colour version of this figure can be viewed online.)

(T^*), also detected in the OR as an enhanced crystal brightness (Fig. 1f), that subsequently triggers the release of acetonitrile (T_I). The latter is possibly associated to an additional structural transition in the **1**•2CH_3CN/CVDG system at T_{III} now detected thanks to the sensitivity of graphene to mechanical and electrostatic changes in the surface. The modification of the magnetic properties concomitant with the structural transition [34] is too subtle to be relevant in the transport properties of graphene.

Finally, the field-effect hole mobility (μ_h) is studied as a function of temperature in the **1**•2CH_3CN/CVDG FET (Fig. 4f). See Section S4 in the Supporting Information for details. Room-temperature μ_h is 602 $cm^2 V^{-1} s^{-1}$, approximately half the value obtained in p-CVDG FETs (1237 $cm^2V^{-1}s^{-1}$). This reduction and mobility values are similar to other reports with crystals or nanoparticles deposited on graphene [24]. Thereafter μ_h steadily decreases with increasing temperature. This behaviour is characteristic of pristine graphene monolayers [24,43]. In contrast, a small increment in μ_h is observed at T_{III} (black arrow in Fig. 4f), probably as a result of adjustments at the **1**•2CH_3CN-graphene interface [24].

We now explore alternative geometries to facilitate the integration of polymeric crystals in graphene devices. For this, we form in-situ a **1**•2CH_3CN/CVDG heterostructure by directly crystallizing **1**•2CH_3CN onto the CVDG FET. First, the reaction of pyrazine with $Fe(BF_4)_2{\cdot}6H_2O$ is carried out in acetonitrile. Thereafter, an uncrystallised solution microdroplet (4–8 μL) is drop-casted onto the pre-cleaned CVDG-FET, where the evaporation of the solvent occurs at a fixed temperature (20 °C). Thereafter, the device is left 40–60 min in ambient conditions to promote in-situ crystallization. An image of the resulting device is shown in Fig. 5a. A yellow film about 300 nm thick is formed fully covering graphene (See Fig. S9 in the Supporting Information for an AFM characterization). A first fingerprint of the crystallinity of the film is obtained in X-ray powder diffraction (XRPD) measurements. Fig. 5b shows the XRPD patterns measured on a bulk polycrystalline **1**•2CH_3CN sample (top) and a **1**•2CH_3CN film (bottom). The diffraction patterns remain very similar and therefore the crystalline phase of the drop-casted **1**•2CH_3CN film is preserved. Besides, Raman spectroscopy on a single-crystal and the film shows identical vibrational modes in both samples. See Fig. S10 in the Supporting Information.

The **1**•2CH_3CN(film)/CVDG FET is thereafter heated up to 363 K while measuring the optical reflectivity (OR). The OR remains initially constant up to $T^* = 303$ K where it slightly increases and the film colour changes to a brighter shade of yellow, as clearly seen in Video S1. Thereafter, OR sharply decreases at $T_I = 309$ K while the colour of the film changes from yellow to orange (see Fig. 5c and Video S1). At 320 K the compound is completely orange and the OR remains stable until the end of the heating cycle. The crystal to crystal transformation and subsequent release of acetonitrile molecules, observed in single crystals, is therefore preserved in the **1**•2CH_3CN film.

Finally, the electrical characterization of the **1**•2CH_3CN(film)/CVDG FET is shown in Fig. 5d. The *I–T* characteristic presents a jump in conductance at $T^* = 303$ K, coincident with the enhanced OR in the film, followed by a sharp drop at $T_I = 309$ K roughly reproducing the results from OR and electron transport measurements in **1**•2CH_3CN/CVDG FETs made with single crystals (Fig. 2). No change in current is observed at T_{II}.

4. Conclusions

In conclusion, we have shown how interfacing npCPs with single-layer graphene can provide a powerful tool to transduce crystal-to-crystal transformations into sizeable electrical signals and vice versa to modulate graphene electronic properties in a controlled way through strain and/or molecular release. For this, a crystalline non-porous coordination polymer (**1**·2CH_3CN) has been interfaced with single-layer

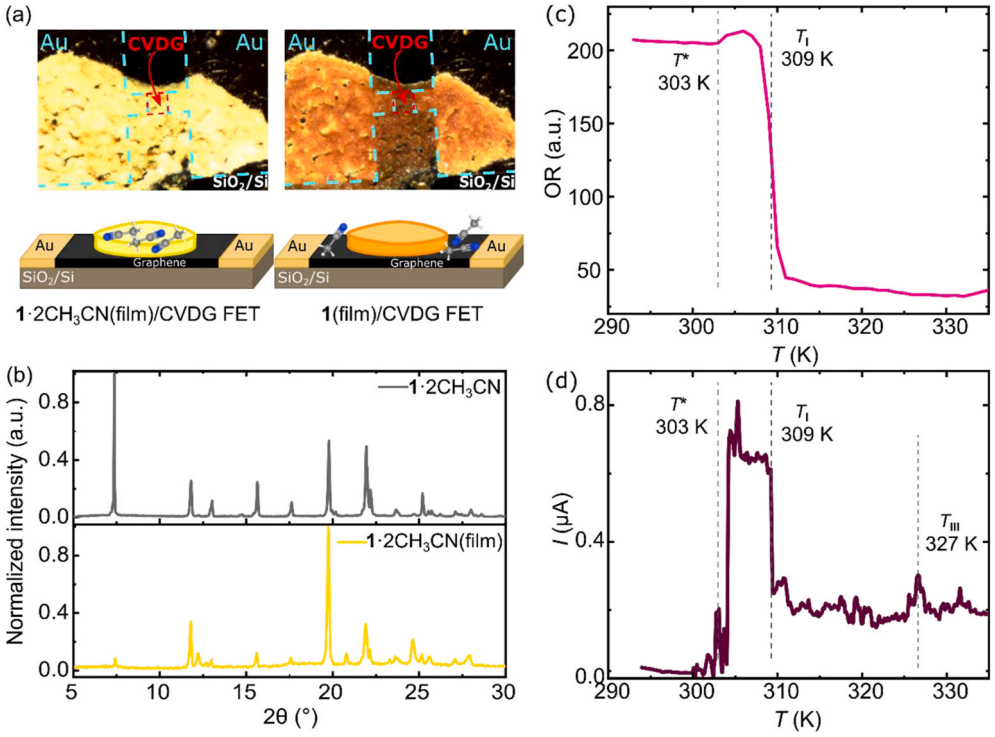

Fig. 5. a) Optical image and schematic representation of a **1**•2CH_3CN(film)/CVDG FET before and after the temperature-induced release of interstitial acetonitrile. b) Room temperature X-ray powder diffraction (XRPD) patterns measured on a **1**•2CH_3CN film (yellow) and a **1**•2CH_3CN polycrystalline reference sample (grey). The diffraction patterns are equivalent. c) Optical reflectivity measured on a **1**•2CH_3CN(film)/CVDG FET as a function of the temperature. A small increment is observed at $T^* = 303$ K followed by a steep drop at $T_I = 309$ K. d) Current-temperature (I–T) characteristic measured at $V_{sd} = 2$ V in a **1**•2CH_3CN(film)/CVDG FET. A sharp increment in conductance at $T^* = 303$ K is followed by a drop at $T_I = 309$ K, in agreement with the optical reflectance and measurements on **1**•2CH_3CN/CVDG FETs based on single crystals (Fig. 2). (A colour version of this figure can be viewed online.)

graphene to form a hybrid **1**·2CH_3CN/graphene field effect transistor. Gate spectroscopy measurements show that the sharp structural transitions in the crystal, and subsequent release of interstitial acetonitrile, occurring at specific temperatures, are translated into a temperature-selective modification of doping and charge carrier mobility in graphene. The current increment at the transitions is orders of magnitude higher than in direct transport across npCP crystals. Besides, the sensitivity of graphene to mechanical and electrostatic changes has surfaced two additional transitions, also at definite temperatures, hinted in the OR but not observed before in transport measurements. Our studies could potentially present applications in cold chain monitoring or for detection of contaminants exceeding a certain threshold and can be extrapolated to other reversible npCPs [2].

Finally, **1**•2CH_3CN has been directly crystallized onto CVDG FETs. The resulting **1**•2CH_3CN films preserve the crystalline phase of single crystals and the optical and electronic transitions observed in hybrid FETs. This method simplifies the integration of npCP in devices and optimizes the interface with graphene or other van der Waals materials.

CRediT authorship contribution statement

Lucía Martín-Pérez: Writing – original draft, Investigation, Formal analysis, Data curation. **Esther Resines-Urien:** Formal analysis, Data curation. **José Sánchez Costa:** Writing – review & editing, Supervision, Resources, Funding acquisition. **Enrique Burzurí:** Writing – review & editing, Supervision, Resources, Methodology, Conceptualization.

Declaration of competing interest

The authors declare that they have no known competing financial interests or personal relationships that could have appeared to influence the work reported in this paper.

Acknowledgements

This work has received support from grants RYC2019-028429-I (EB), TED2021-130957B-C55 (EB), PID2020114653RB-I00 (JSC) and TED2021-131018B-C22 (JSC) funded by MCIN/AEI/10.13039/501100011033 and the MAD2D-CM-MRR MATERIALES AVANZADOS-IMDEA NC. IMDEA Nanociencia acknowledges support from the 'Severo Ochoa' Programme for Centres of Excellence in R&D (MINECO, Grant CEX2020-001039-S) and the NANOMAGCOST (P2018/NMT4321). EB acknowledges the "María de Maeztu" Programme for Units of Excellence in R&D (CEX2018-000805-M).

Appendix A. Supplementary data

Supplementary data to this article can be found online at https://doi.org/10.1016/j.carbon.2024.119145.

References

[1] H. Furukawa, K.E. Cordova, M. O'Keeffe, O.M. Yaghi, Science (80-.) 341 (2013) 1230444.
[2] J. Sánchez Costa, S. Rodríguez-Jiménez, G.A. Craig, B. Barth, C.M. Beavers, S. J. Teat, G. Aromí, J. Am. Chem. Soc. 136 (2014) 3869–3874.
[3] E. Coronado, M. Giménez-Marqués, G.M. Espallargas, L. Brammer, Nat. Commun. 3 (2012) 828.
[4] Y. Cui, Y. Yue, G. Qian, B. Chen, Chem. Rev. 112 (2012) 1126–1162.
[5] J. López-Cabrelles, S. Mañas-Valero, I.J. Vitórica-Yrezábal, M. Šiškins, M. Lee, P. G. Steeneken, H.S.J. Van Der Zant, G. Mínguez Espallargas, E. Coronado, J. Am. Chem. Soc. 143 (2021) 18502–18510.
[6] J. González, P. Sevilla, G. Gabarró-Riera, J. Jover, J. Echeverría, S. Fuertes, A. Arauzo, E. Bartolomé, E.C. Sañudo, Angew. Chem. Int. Ed. 60 (2021) 12001–12006.
[7] L. Piñeiro-López, F.J. Valverde-Muñoz, E. Trzop, M.C. Muñoz, M. Seredyuk, J. Castells-Gil, I. da Silva, C. Martí-Gastaldo, E. Collet, J.A. Real, Chem. Sci. 12 (2021) 1317–1326.
[8] C. Boix-Constant, V. García-López, E. Navarro-Moratalla, M. Clemente-León, J. L. Zafra, J. Casado, F. Guinea, S. Mañas-Valero, E. Coronado, Adv. Mater. 34 (2022) 2110027.
[9] H. Li, L. Li, R.B. Lin, W. Zhou, Z. Zhang, S. Xiang, B. Chen, Inside Energy 1 (2019) 100006.
[10] E. Resines-Urien, L. Piñeiro-López, E. Fernandez-Bartolome, A. Gamonal, M. Garcia-Hernandez, J. Sánchez Costa, Dalton Trans. 49 (2020) 7315–7318.
[11] S. Rodríguez-Jiménez, H.L.C. Feltham, S. Brooker, Angew. Chem. Int. Ed. 55 (2016) 15067–15071.
[12] T. Qiu, Z. Liang, W. Guo, H. Tabassum, S. Gao, R. Zou, ACS Energy Lett. 5 (2020) 520–532.
[13] L.S. Xie, G. Skorupskii, M. Dincă, Chem. Rev. 120 (2020) 8536–8580.
[14] V. Rubio-Giménez, S. Tatay, C. Martí-Gastaldo, Chem. Soc. Rev. 49 (2020) 5601–5638.
[15] C. Avendano, Z. Zhang, A. Ota, H. Zhao, K.R. Dunbar, Angew. Chem. Int. Ed. 50 (2011) 6543–6547.
[16] D. Sheberla, L. Sun, M.A. Blood-Forsythe, S. Er, C.R. Wade, C.K. Brozek, A. Aspuru-Guzik, M. Dincă, J. Am. Chem. Soc. 136 (2014) 8859–8862.
[17] R. Dong, P. Han, H. Arora, M. Ballabio, M. Karakus, Z. Zhang, C. Shekhar, P. Adler, P.S. Petkov, A. Erbe, S.C.B. Mannsfeld, C. Felser, T. Heine, M. Bonn, X. Feng, E. Cánovas, Nat. Mater. 17 (2018) 1027–1032.
[18] A.A. Talin, A. Centrone, A.C. Ford, M.E. Foster, V. Stavila, P. Haney, R.A. Kinney, V. Szalai, F. El Gabaly, H.P. Yoon, F. Léonard, M.D. Allendorf, Science (80-.) 343 (2014) 66–69.
[19] J.H. Dou, M.Q. Arguilla, Y. Luo, J. Li, W. Zhang, L. Sun, J.L. Mancuso, L. Yang, T. Chen, L.R. Parent, G. Skorupskii, N.J. Libretto, C. Sun, M.C. Yang, P.V. Dip, E. J. Brignole, J.T. Miller, J. Kong, C.H. Hendon, J. Sun, M. Dincă, Nat. Mater. 20 (2020) 222–228.
[20] K.S. Novoselov, A. Mishchenko, A. Carvalho, A.H. Castro Neto, Science (80-.) 353 (2016) aac9439.
[21] R. Wang, X.G. Ren, Z. Yan, L.J. Jiang, W.E.I. Sha, G.C. Shan, Front. Physiol. 14 (2019) 13603.
[22] K. Kostarelos, K.S. Novoselov, Nat. Nanotechnol. 9 (2014) 744–745.
[23] J.F. Dayen, N. Konstantinov, M. Palluel, N. Daro, B. Kundys, M. Soliman, G. Chastanet, B. Doudin, Mater. Horiz. 8 (2021) 2310–2315.
[24] J. Dugay, M. Aarts, M. Giménez-Marqués, T. Kozlova, H.W. Zandbergen, E. Coronado, H.S.J. van der Zant, Nano Lett. 17 (2017) 186–193.
[25] N. Konstantinov, A. Tauzin, U.N. Noumbé, D. Dragoe, B. Kundys, H. Majjad, A. Brosseau, M. Lenertz, A. Singh, S. Berciaud, M.L. Boillot, B. Doudin, T. Mallah, J. F. Dayen, J. Mater. Chem. C 9 (2021) 2712–2720.
[26] E.P. Geest, K. Shakouri, W. Fu, V. Robert, V. Tudor, S. Bonnet, G.F. Schneider, Adv. Mater. 32 (2020) 1903575.
[27] P. Solís-Fernández, M. Bissett, H. Ago, Chem. Soc. Rev. 46 (2017) 4572–4613.
[28] W. Fu, L. Jiang, E.P. van Geest, L.M. C Lima, G.F. Schneider, W. Fu, L. Jiang, E. P. van Geest, L.M. C Lima, G.F. Schneider, Adv. Mater. 29 (2017) 1603610.
[29] Y. Zheng, S. Zheng, H. Xue, H. Pang, Y. Zheng, S. Zheng, H. Xue, H. Pang, Adv. Funct. Mater. 28 (2018) 1804950.
[30] K. Wang, K.N. Hui, K. San Hui, S. Peng, Y. Xu, Chem. Sci. 12 (2021) 5737–5766.
[31] T.T. Tung, M.T. Tran, J.F. Feller, M. Castro, T. Van Ngo, K. Hassan, M.J. Nine, D. Losic, Carbon N. Y. 159 (2020) 333–344.
[32] J. Sánchez Costa, S. Rodríguez-Jiménez, G.A. Craig, B. Barth, C.M. Beavers, S. J. Teat, K.J. Gagnon, L.A. Barrios, O. Roubeau, G. Aromí, Inorg. Chem. Front. 7 (2020) 3165–3175.
[33] A. Develioglu, E. Resines-Urien, R. Poloni, L. Martín-Pérez, J. Sanchez Costa, E. Burzurí, Adv. Sci. 8 (2021) 2102619.
[34] E. Resines-Urien, E. Burzurí, E. Fernandez-Bartolome, M.Á. García García-Tuñón, P. De La Presa, R. Poloni, S.J. Teat, J. Sánchez Costa, Chem. Sci. 10 (2019) 6612–6616.
[35] J. Villalva, A. Develioglu, N. Montenegro-Pohlhammer, R. Sánchez-de-Armas, A. Gamonal, E. Rial, M. García-Hernández, L. Ruiz-Gonzalez, J. Sánchez Costa, C. J. Calzado, E.M. Pérez, E. Burzurí, Nat. Commun. 12 (2021) 1578.
[36] P.K. Srivastava, P. Yadav, V. Rani, S. Ghosh, ACS Appl. Mater. Interfaces 9 (2017) 5375–5381.
[37] R. Obertík, J. Chudoba, J. Šturala, J. Tarábek, L. Ludvíková, T. Slanina, B. König, R. Cibulka, Chem. Eur J. 28 (2022) e202202487.
[38] S. Ryu, L. Liu, S. Berciaud, Y.J. Yu, H. Liu, P. Kim, G.W. Flynn, L.E. Brus, Nano Lett. 10 (2010) 4944–4951.
[39] Q.H. Wang, Z. Jin, K.K. Kim, A.J. Hilmer, G.L.C. Paulus, C.J. Shih, M.H. Ham, J. D. Sanchez-Yamagishi, K. Watanabe, T. Taniguchi, J. Kong, P. Jarillo-Herrero, M. S. Strano, Nat. Chem. 49 (4) (2012) 724–732, 2012.
[40] M. Vázquez Sulleiro, A. Develioglu, R. Quirós-Ovies, L. Martín-Pérez, N. Martín Sabanés, M.L. Gonzalez-Juarez, I.J. Gómez, M. Vera-Hidalgo, V. Sebastián, J. Santamaría, E. Burzurí, E.M. Pérez, Nat. Chem. 14 (2022) 695–700.
[41] T. Feng, D. Xie, G. Li, J. Xu, H. Zhao, T. Ren, H. Zhu, Carbon N. Y. 78 (2014) 250–256.
[42] J.E. Lee, G. Ahn, J. Shim, Y.S. Lee, S. Ryu, Nat. Commun. 3 (2012) 1024.
[43] W. Zhu, V. Perebeinos, M. Freitag, P. Avouris, Phys. Rev. B Condens. Matter 80 (2009) 235402.